Journal of Engineering Mathematics **47:** 369–386, 2003.

Blood-flow models of the circle of Willis from magnetic resonance data

JUAN R. CEBRAL[1], MARCELO A. CASTRO[1], ORLANDO SOTO[1], RAINALD LÖHNER[1] and NOAM ALPERIN[2]
[1]*School of Computational Sciences, George Mason University, Fairfax, Virginia, USA;* [2]*Department of Radiology, University of Illinois at Chicago, Chicago, Illinois, USA*

Received 6 February 2003; accepted in revised form 18 August 2003

Abstract. Detailed knowledge of the cerebral hemodynamics is important for a variety of clinical applications. Cerebral perfusion depends not only on the status of the diseased vessels but also on the patency of collateral pathways provided by the circle of Willis. Due to the large anatomical and physiologic variability among individuals, realistic patient-specific models can provide new insights into the cerebral hemodynamics. This paper presents an image-based methodology for constructing patient-specific models of the cerebral circulation. This methodology combines anatomical and physiologic imaging techniques with computer simulation technology. The methodology is illustrated with a finite element model constructed from magnetic resonance image data of a normal volunteer. Several of the remaining challenging problems are identified. This work represents a starting point in the development of realistic models that can be applied to the study of cerebrovascular diseases and their treatment.

Key words: circle of Willis, computational fluid dynamics, hemodynamics, magnetic resonance

1. Introduction

Stroke is the third leading cause of death after heart disease and cancer and the leading cause of long-term disability in Western world [1]. Ischemic infarction of the brain can occur due to diminution of cerebral blood flow below a certain threshold, sudden occlusion of a feeding artery, rupture of an intracranial aneurysm, embolic phenomena or surgical maneuvers [1]. Cerebral perfusion depends not only on the status of the diseased vessels but also on the patency of collateral pathways [2]. The primary collateral pathway is the collateral flow provided by the circle of Willis [3]. Detailed knowledge of the cerebral hemodynamics is important for a variety of clinical applications [4–6]. For instance, analysis of blood-flow alterations during arterial occlusions or endovascular interventions such as angioplasty and stenting, correlation of regions of disturbed flow with occurrence of embolic phenomena, correlation of regions of low wall shear stress with development of intracranial aneurysms, etc. Over the years, numerous idealized computer models of the cerebral circulation have been developed and used to study some of these questions [7]. However, anatomical variability among individuals is large. Only about 40% of the population has a complete, well-balanced circle of Willis as the ones shown in anatomy textbooks [8, Chapter 25]. Realistic patient-specific models that can provide new insight into the cerebral hemodynamics have only recently been attempted [5]. Image-based computational-fluid-dynamics (CFD) techniques have recently been developed and applied to a variety of hemodynamics problems [9–12]. The purpose of this paper is to describe recent advances towards a methodology to construct patient-specific

models of the cerebral circulation from medical image data and at the same time identify challenging problems that remain to be solved. This work represents a starting point in the development of a realistic modeling methodology that will incorporate arterial networks beyond the circle of Willis, secondary collateral pathways, autoregulation mechanisms and models of tissue perfusion. The significance is that these numerical simulations can potentially be used for studying a variety of cerebrovascular diseases and for evaluation of possible treatments.

2. Methods

2.1. Medical image data

In order construct realistic patient-specific models of the cerebral arterial system it is necessary not only to create realistic anatomical models but also to prescribe the correct physiologic flow conditions. To this end, both 3D anatomical images and physiologic measurements must be obtained. Magnetic-resonance angiography (MRA) images typically consist in a stack of 2D slices of constant width covering the volume of interest. In the images obtained in this way arteries appear whiter than the surrounding tissue. Typical image sizes are approximately 100 slices of 512×512 or 256×256 pixels. The voxel (three-dimensional pixel) intensity is encoded in 16 bits unsigned integers. Reconstruction of arterial models from these images is a challenging problem due to noise, limited resolution and image artifacts [13].

Physiologic flow-velocity measurements can be obtained non-invasively using phase-contrast magnetic-resonance (PC-MR) techniques. Although PC-MR techniques allow for the measurement of the flow velocity field in a 3D volume [14], such measurements require very long acquisition times, which carries an associated high level of discomfort to the patient. For this reason typical *in vivo* measurements consist in imaging only one component of the velocity vector on a fixed 2D slice location [15]. In order to measure arterial flow rates, the slice plane is placed more or less perpendicularly to the vessel axis and only the normal component of the velocity is imaged. The PC-MR datasets consist in a series of images obtained during the cardiac cycle. For each instant of time, a pair of images is obtained. One is the magnitude image depicting the anatomy and the other encodes the local tissue velocity. Since the images are acquired over several cardiac cycles, peripheral cardiac gating is used to synchronize the measurements. In the final image an average over several cardiac cycles is performed for each time frame. Typical image size is 20 or 32 phases (time frames) of 256×256 pixels. The magnitude and phase images use 16 bits signed integers to encode the pixel values. Spatial and temporal resolution, and image artifacts limit the accuracy of these measurements. Accurate measurement of blood-velocity profiles remains a challenging problem, especially in small arteries and regions of disturbed flows [16].

2.2. Anatomical modeling

The first step in any CFD simulation is to generate a computational grid. Due to their geometrical flexibility, we use unstructured grids composed of tetrahedral elements. Unstructured grid generation requires the specification of the geometry of the computational domain. In most engineering applications, this is done using analytical surface patches [17]. However, in cases when the geometry is obtained from some kind of measurement, we prefer to work directly with the discrete data [18] (*e.g.* surface triangulations, cloud of points, etc). This approach does not require the extra step of fitting analytical surfaces to the discrete data. On the other

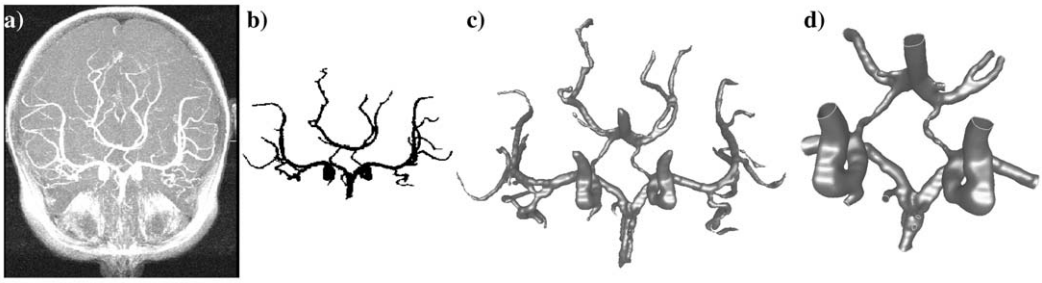

Figure 1. Model of the circle of Willis reconstructed using a region growing approach: a) MRA images; b) segmented vessels; c) tessellated surface; d) final anatomical model after smoothing and cutting.

hand, it is necessary to implement several geometrical operations for surface triangulations, which are not typically available in commercial software packages.

The simplest method to reconstruct models of the cerebrovasculature from MRA images consists in the following image processing operations [19]. First, the contrast of the image is increased (sharpen operation) in order to reduce the image noise. Then, a region-growing segmentation is used to recursively label voxels that are connected to a given seed voxel and with "similar" intensity. The success of this method depends on the appropriate choice of the intensity threshold used to define "similar" intensities. This is done by trial and error. Once all the voxels inside the desired arteries have been labeled, a surface triangulation is created either by extracting an intensity iso-surface or by direct tessellation of the labeled voxel faces. This technique is very straightforward to implement and easy to automate. However, it may yield topological defects such as self-intersecting surfaces and holes, or produce inaccurate results in regions where the image intensity is not homogeneous inside the vessels. Some solutions to these problems are available [19]. An example of this anatomical reconstruction methodology is presented in Figure 1. The maximum intensity projection (MIP) of the MRA images is shown in Figure 1a. The MIP of these images after region growing segmentation of vessels is shown in Figure 1b. The geometrical model extracted from these segmented images is shown in Figure 1c. Note some topological defects (vessel intersections) created in some of the small vessels. The final model after smoothing and interactive cutting is shown in Figure 1d.

A second alternative, which has proven accurate and very robust, is a component-based approach [20]. In this case, each arterial branch is reconstructed independently using a deformable model [13]. First the axis of each vessel is manually selected on cross-sectional views. Then, a cylindrical surface triangulation is constructed along the vessel axis. Each node of this surface is then allowed to move in the radial direction under the action of internal and external forces. Neighboring nodes exert internal elastic forces (spring analogy) that tend to smooth the surface. External forces computed from the image energy gradient are also applied. These external forces tend to localize the surface nodes at the edges of the artery. The image gradients are computed by convolution with the derivatives of a Gaussian kernel and interpolated to the position of the surface nodes. Once all the arterial branches have been reconstructed, a watertight surface model is generated using a surface-merging algorithm [21]. This algorithm first creates a background grid that covers the entire computational domain. Then, the shortest distance from each point in the background grid to any reconstructed surface is calculated and assigned positive or negative values if the point lies inside or outside this closest surface. The background grid is adaptively refined in regions close to the vessel surfaces in order to increase the resolution of the algorithm. A zero-level iso-surface is then extracted from

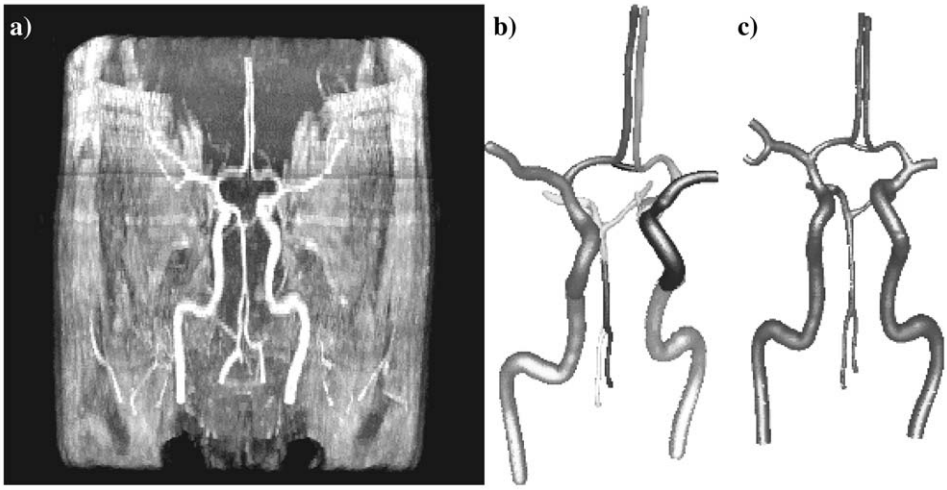

Figure 2. Model of the circle of Willis reconstructed using a component-based approach: a) MRA images; b) model components reconstructed using a tubular deformable model; c) final model after merging individual components and smoothing.

the signed distance map computed on the adapted background grid. This approach produces accurate results [22] and the topological defects created by the previous method are avoided by increasing the background-grid resolution in regions of close vessels. An example of this methodology is presented in Figure 2. The MIP of the MRA images is shown in Figure 2a. The arterial branches reconstructed independently are shown in Figure 2b with different colors, and the final model after merging, smoothing and cutting is shown in Figure 2c.

Before proceeding to the unstructured grid generation, the surface model reconstructed by either method is further processed. The quality of the surface triangulation is optimized using a combination of edge collapsing and diagonal swapping algorithms [19] to delete too small or very stretched elements and to minimize the maximum internal angle. Small-scale imperfections are removed using a non-shrinking surface-smoothing algorithm [23]. Finally, the model is interactively cut perpendicularly to the vessel axis at selected locations where boundary conditions will be imposed, for instance at the locations where flow measurements were performed. The final triangulation is then used as a support surface to define the computational domain. An advancing-front technique [24] is used to generate a new surface triangulation and then to fill the interior of the volume. During the surface-grid generation, a fast neighbor-to-neighbor interpolation algorithm [24] is used to position newly created points on the support surface. Topological constraints are imposed in order to avoid jumps between close arterial branches. That is, a point is connected to the current "active front edge" only if it is possible to march on the surface from the edge to the point [12]. The use of source functions to specify the desired element-size distribution can become very tedious in cases involving many arterial branches of different sizes. A more advantageous approach is to use background grids that are adaptively refined in regions of high surface curvature [12]. This approach yields meshes that have roughly a uniform number of elements across any cross-section of the computational domain. An example is presented in Figure 3. Figure 3a shows the surface of the finite-element grid generated using sources to increase the resolution along some of the smaller arterial branches. This grid, which contained roughly 4 million elements, corresponds to the model shown in Figure 1. A finite-element grid generated using an adaptive

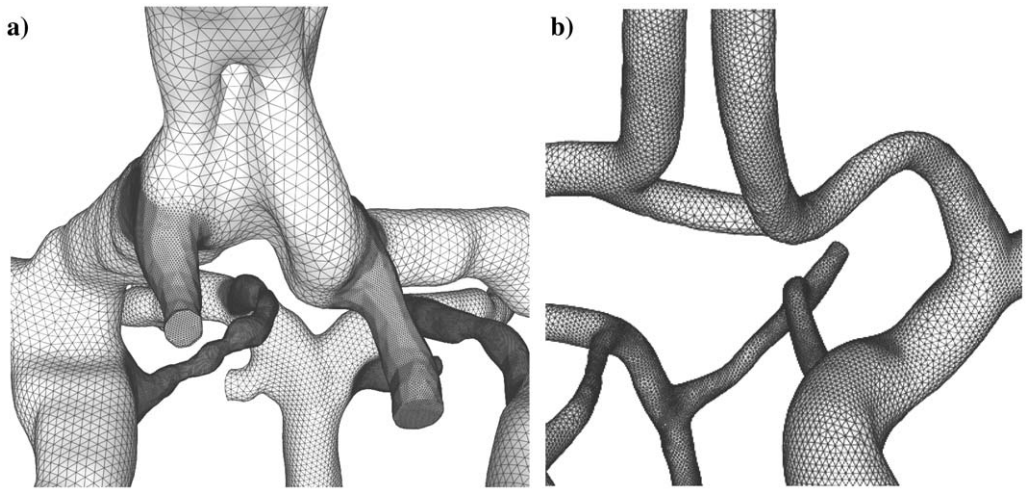

Figure 3. Detail of the surface of the finite-element grids generated using sources (a) and adaptive background grids (b) to specify the element size distribution.

background grid is shown in Figure 3b. This grid corresponds to the model of Figure 2 and contained roughly 1 million elements.

2.3. Blood-flow modeling

Blood is mathematically modeled as a time-dependent viscous incompressible fluid [25, Chapter 1]. The governing equations that express the conservation of mass and momentum are:

$$\nabla \cdot \mathbf{v} = 0, \tag{1}$$

$$\rho \left(\frac{\partial \mathbf{v}}{\partial t} + \mathbf{v} \cdot \nabla \mathbf{v} \right) = \nabla \cdot \boldsymbol{\sigma}, \tag{2}$$

where ρ is the density and $\mathbf{v}(\mathbf{x},t)$ the velocity field. The stress tensor $\boldsymbol{\sigma}$ can be written as:

$$\boldsymbol{\sigma} = -p\,\mathbf{1} + \boldsymbol{\tau}, \tag{3}$$

where p is the pressure, $\mathbf{1}$ the unit tensor and $\boldsymbol{\tau}$ the anisotropic or deviatoric stress tensor. The strain-rate tensor is defined as

$$\boldsymbol{\varepsilon} = \frac{1}{2} \left(\nabla \mathbf{v} + \nabla^T \mathbf{v} \right). \tag{4}$$

Then, the deviatoric stress tensor for a Newtonian fluid is written as

$$\boldsymbol{\tau} = \frac{1}{2} \mu\, \boldsymbol{\varepsilon} \tag{5}$$

where μ is the viscocity. It is known that, since blood consists in a suspension of particles (red blood cells, white blood cells, platelets) in an aqueous medium, it behaves as a non-Newtonian fluid. Although typically neglected for large arteries, recent studies [26] suggest

that non-Newtonian effects may be important in regions of low flow and during some portions of the cardiac cycle [20]. In addition, the use of non-Newtonian models does not increase the computing time substantially. Therefore, to be on the safe side we prefer to always include these effects. The non-Newtonian behavior of blood is commonly approximated using the model of Casson [25, Chapter 5], which is usually written as a scalar relationship between the shear stress τ and the strain rate $\dot{\gamma}$ of the form

$$\sqrt{\tau} = \sqrt{\mu\,\dot{\gamma}} + \sqrt{\tau_0}, \tag{6}$$

where τ_0 is the yield stress. The strain rate is derived from the second invariant of the strain rate tensor [27], which for incompressible fluids becomes

$$\dot{\gamma} = 2\sqrt{tr(\varepsilon^2) - tr(\varepsilon)^2} = 2\sqrt{\varepsilon_{ij}\,\varepsilon_{ij}}. \tag{7}$$

The viscocity in Equation (5) is constant for Newtonian fluids. For the Casson model, it is assumed that Equation (5) still holds, but now the "apparent" viscocity μ' is variable and can be computed from Casson's formula (Equation (6))

$$\mu' = \left(\sqrt{\mu} + \sqrt{\tau_0/\dot{\gamma}}\right)^2. \tag{8}$$

Since this expression diverges for zero strain rates (region of plug flow), a modified version is used [28]:

$$\mu' = \left(\sqrt{\mu} + \sqrt{\tau_0(1 - \mathrm{e}^{-m\,\dot{\gamma}})/\dot{\gamma}}\right)^2. \tag{9}$$

This modification effectively imposes a cutoff on the viscocity and the parameter m in this equation controls the maximum viscocity attainable in the plug region.

The values of the model parameters typically used for blood flows are: $\rho = 1{\cdot}1$ g/cm^3, $\mu = 0{\cdot}04$ Poise, $\tau_0 = 0{\cdot}04$ dyne/cm^2, $m = 100$.

The numerical solution of the governing equations is obtained using an implicit stabilized finite-element method [29]. The finite-element formulation can be written in an Arbitrary Lagrangian Eulerian (ALE) reference frame as

$$\begin{aligned} &\tfrac{1}{\delta t}\left((\mathbf{v}^{n+1,i}, \mathbf{w}) - (\mathbf{v}^n, \mathbf{w})_{\Omega^n}\right) + (\mathbf{u}^{n+\theta,i-1}\cdot\nabla\mathbf{v}^{n+\theta,i}, \mathbf{w}) + (\nu\,\nabla\mathbf{v}^{n+\theta,i}, \nabla\mathbf{w}) \\ &-(p^{n+1,i-1}, \nabla\cdot\mathbf{w}) + (\tau\,(\mathbf{u}^{n+\theta,i-1}\cdot\nabla\mathbf{v}^{n+\theta,i} - \alpha\,\pi^{n+\theta,i-1}), \mathbf{u}^{n+\theta,i-1}\cdot\nabla\mathbf{w}) \\ &\qquad = (\mathbf{f}^{n+\theta}, \mathbf{w}) + (\sigma^{n+\theta,i-1}\cdot\mathrm{n}, \mathbf{w})_\Gamma, \end{aligned} \tag{10}$$

$$\delta\,t\,(\nabla p^{n+1,i} - \nabla p^{n+1,i-1}, \nabla q) + (\tau\,(\nabla p^{n+1,i} - \alpha\,\xi^{n+1,i-1}), \nabla q) = -(\nabla\cdot\mathbf{v}^{n+1,i}, q), \tag{11}$$

$$(\pi^{n+\theta,i}, \mathbf{w}) = (\mathbf{u}^{n+\theta,i}\cdot\nabla\mathbf{v}^{n+\theta,i}, \mathbf{w}), \tag{12}$$

$$(\xi^{n+1,i}, \mathbf{w}) = (\nabla p^{n+1,i}, \mathbf{w}), \tag{13}$$

where the superscript n is the time-step level, θ the trapezoidal rule parameter, i the sub-iteration level, $\mathbf{w}$ and q the finite-element test functions, δt the time-step size, $\nu = \mu/\rho$ the kinematic viscocity, **f**the external forces, $\boldsymbol{\sigma}$ the deviatoric stress tensor, $\mathbf{u} = \mathbf{v} - \mathbf{v}_m$ is the advective velocity and $\mathbf{v}_m$ the mesh velocity; π and ξ are the projections of the advective and pressure gradient terms on to the finite element space, respectively. Further, Γ is the boundary

of the computational domain Ω, n its outer normal, and (a, b) denotes the L^2 inner product, taken in the current domain Ω^{n+1} unless otherwise specified. The local critical time-step τ is computed in each element according to the Courant-Friedrich-Levy (CFL) criterion

$$\tau = \frac{h^2}{4\,\nu + 2\,|\mathbf{u}|h}, \tag{14}$$

where h is the element size. The discretized momentum Equation (10) is solved using a diagonal preconditioned Generalized Minimal Residual (GMRES) algorithm, while the pressure Equation (11) is solved using a conjugate gradient method [30, Chapters 5, 6]. The projected terms (12) and (13) are treated explicitly using a lumped approximation of the mass matrix. The algorithm is repeated until convergence in each time-step. Using linear elements, the convective stabilization is no more than a second order Streamline Diffusion. This term is obtained by adding to the standard Galerkin terms, the integral over the domain of the convective operator applied to the velocity test function, times the parameter τ (intrinsic time), and times the difference between the convective term and its projection onto the finite-element space. This difference represents the orthogonal projection of the convective contribution onto the finite-element space. For the pressure Equation (incompressibility condition) the same idea is used: the stabilizing term is the pressure operator applied to its respective test function, times the intrinsic time, times the orthogonal projection of the pressure terms onto the finite-element space. It can be checked that such a contribution is at least a fourth-order term $O(h^4)$. The boundary conditions for the velocities are the standard ones: Velocities are prescribed at the inlets and at the vessel walls, and the viscous stresses are set to zero at the outlets in a weak form. The pressures may be left free in the whole boundary. This is possible due to the convergence of the whole scheme to a monolithic solution at each time step, and to the standard preconditioned GMRES solver that is being utilized for the discrete momentum equations. However, the standard practice is to set the pressures in a strong form at the outflows, which provides a faster convergence of the iterative scheme. On the rest of the boundary, it can be checked that the boundary term for the pressure Poisson equation that are neglected are of order $O(h^4)$, which maintains the second-order accuracy of the standard Galerkin formulation $O(h^2)$.

Since this scheme is unconditionally stable, arbitrary time-step sizes can be selected. Typically 100–400 time-steps per cardiac cycle are used. A pressure switch term of the form

$$\alpha = 1 - \frac{\|\nabla p - \xi\|}{\|\nabla p\| + \|\xi\|} \tag{15}$$

was added to the finite-element formulation to reduce the order of the scheme in regions where the pressure gradient is not smooth. Although a term like this was not strictly required for the current applications, it was found necessary for other bio-fluids applications with higher Reynolds numbers in order to achieve convergence in the time-step.

2.4. Physiologic modeling

It is still a matter of debate how important is to incorporate arterial wall compliance in models used to compute hemodynamic quantities such as wall shear stress and oscillatory shear index [31]. The elasticity of healthy arteries significantly affects the shape of the flow waveform and may be important for determining the size of regions of low wall shear stress [20,32]. Arterial wall compliance may be less important in atherosclerotic arteries because of the loss

of elasticity due to the disease [33]. However, no definitive evidence on the importance (or not) of compliance effects has been shown to date. The finite-element method described in the previous section has been used in combination with fluid-solid coupling algorithms to compute blood flows in compliant arterial models [32]. In these cases, the fluid and solid solutions were simultaneously advanced in time by different solvers that exchange information at the fluid-solid boundary. An iterative under-relaxation technique was used to converge to the coupled solution at each time-step. Due to a lack of direct *in vivo* measurements (invasive), the pressure waveform needed to impose boundary conditions was derived from flow measurements using lumped parameter models [32]. However, for simplicity and to reduce computational costs, we assumed rigid arterial walls for the current applications. Future studies will incorporate vessel compliance.

Velocity boundary conditions are derived from *in vivo* measurements of flow rates using PC-MR images. Flow rate curves are obtained by integration of the velocity profile over the cross section of the vessel. The main difficulty here is to identify the pixels that belong to a given vessel. For this purpose, we have used the following three approaches:

a) Manual segmentation [22]: the region of integration is interactively drawn on the PC-MR images (ellipsoidal regions or individual selection of pixels).
b) Threshold segmentation [22]: a threshold segmentation algorithm is used on the magnitude images to define the vessel lumen.
c) Cross-correlation segmentation [34]: a region growing segmentation is used to recursively select pixels if the cross-correlation between the time-dependent flow rate curve through that pixel and that through a seed pixel is above a certain threshold. The optimum threshold value can be automatically calculated by searching for the inflexion point in the histogram of number of selected pixels *vs.* threshold values. The process is illustrated in Figure 4. Figures 4a and 4b show the magnitude and phase images at a selected time frame. Figure 4c shows the selection of a seed pixel in the cropped region of the right internal carotid artery. Figure 4d shows a pixel inside the vessel lumen. Figure 4f shows the flow waveforms through the pixels selected in Figures 4c and 4d. The selected pixels defining the vessel lumen are shown in Figure 4e and the corresponding flow rate is shown in Figure 4g.

Once reconstructed, the flow rate curves are decomposed into N Fourier modes:

$$Q(t) = \sum_{n=0}^{N} Q_n \exp(\mathrm{i}\omega n\, t), \tag{16}$$

where ω is the fundamental angular frequency. This is done under the assumption that the flow is periodic in time. Then, the velocity profile prescribed at the model boundary is obtained as a superposition of Womersley [35,36] velocity profiles:

$$\mathrm{v}(r,t) = \frac{2Q_0}{\pi a^2}\left[1-(r/a)^2\right] + \sum_{n=1}^{N} \frac{Q_n}{\pi a^2}\left[\frac{1 - J_0(\beta_n r/a)\big/ J_0(\beta_n)}{1 - 2J_1(\beta_n)\big/\beta_n J_0(\beta_n)}\right]\exp(\mathrm{i}\omega n\, t), \tag{17}$$

where a is the vessel radius, $\alpha = a\sqrt{\omega/\nu}$ is the Womersley number, $\beta = \mathrm{i}^{3/2}\alpha$, and J_0 and J_1 are the Bessel functions of the first kind. These boundary conditions assume that the flow is fully developed, which is not unreasonable in long arteries with small curvature. The effects of this assumption can be minimized by extruding the model in/outflow boundaries.

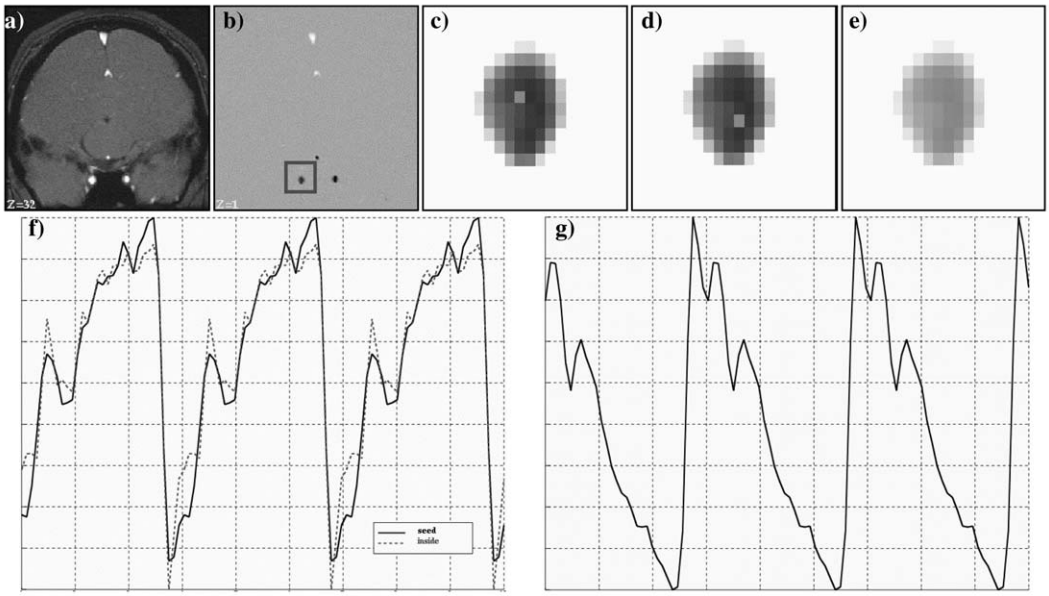

Figure 4. Method for measuring flow rates from PC-MR images: a) magnitude image; b) phase image; c) seed pixel; d) pixel inside the vessel lumen; e) segmented vessel lumen; f) flow waveforms through the pixels selected in c and d; g) flow-rate curve computed on the segmented vessel.

Under normal conditions, four feeding vessels supply the circle of Willis: two internal carotids and two vertebral arteries [3,8]. The flow rates in these vessels can be measured by PC-MR techniques and used to impose inflow boundary conditions during the solution of the flow equations. Furthermore, in many cases all these flows can be measured with only one PC-MR slice. However, in general it is difficult to measure flow rates in all the efferent vessels of the circle of Willis. This would require MRI exams that are too long and the flow measurements in some of the smaller vessels may not be very reliable. Therefore, in such cases the outflow boundary conditions must be derived using models of the distal vascular bed. Vascular bed models used in the past to impose outflow boundary conditions for hemodynamics calculations include: series of resistors in parallel [5], structured fractal trees [37], porous media [6], etc. A more realistic approach we are currently investigating consists in coupling the 3D finite-element model to 1D flow models [38] along arterial trees generated for each outflow boundary. These arterial trees are generated using an image-based constrained constructive optimization method [39]. For a given perfusion volume and a feeding artery, an arterial tree that supplies the entire volume is grown in such a way as to minimize the intravascular volume. These trees exhibit geometrical properties such as bifurcation angles, area and symmetry ratios, which are statistically in agreement with experimental observations [40]. The main difficulty lies in the definition of the perfusion volume for each outlet of the finite-element model. Currently this is done by manual labeling of voxels on MRI images of the brain. These vascular trees have the advantages that the perfusion volume can be subdivided into regions of different vessel density (*e.g.* gray and white matter), collateral vessels joining adjacent arterial trees can be easily generated, and autoregulation models that dilate or constrict certain portions of the tree can be easily incorporated. An example of the procedure is presented in Figure 5. The top row shows the brain MRI images used to manually define the perfusion volumes of the left anterior cerebral artery (ACA) and the left middle cerebral artery

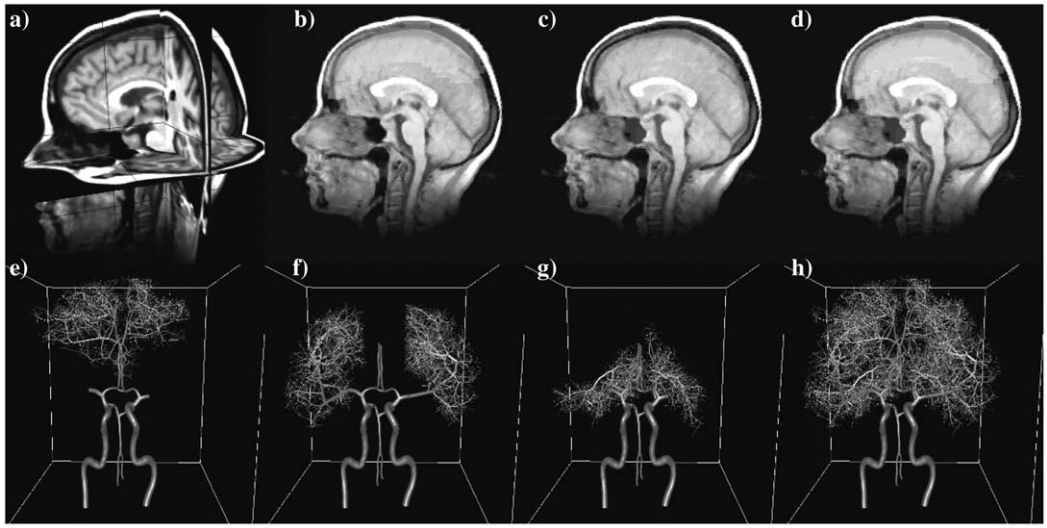

Figure 5. Construction of arterial tree models: a) MRI images of the brain; b) perfusion region of the left ACA; c) perfusion volume of the left MCA; d) superposition of the perfusion regions of the left ACA and MCA; e) tree models for the ACAs; f) tree models for the MCAs; g) tree models for the PCAs; h) tree model for all efferent vessels of the circle of Willis.

(MCA). The bottom row shows the arterial trees generated for each of the efferent vessels of the finite-element model of Figure 2. Statistics of the geometrical properties of these trees are presented in Figure 6. These plots show for each segment in the tree the symmetry ratio (a), area ratio (b), bifurcation angle (c), and length-to-radius ratio. In agreement with experimental observations [40], these trees exhibit no symmetry or fractal properties.

2.5. Blood-flow visualization

The large amounts of data generated during pulsatile blood flow calculations are visualized using classic visualization techniques such as vector plots, contour plots, particle traces, iso-surfaces, etc. In addition, a few hemodynamic quantities of interest are computed in a post-processing stage under the assumption of flow periodicity. For instance the tangential stress vector (tangential force per unit area) on the arterial wall is obtained from the deviatoric stress tensor:

$$\mathbf{f} = \boldsymbol{\tau} \cdot \mathbf{n}, \tag{18}$$

where $\mathbf{n}$ is the normal to the wall. Then, the mean wall shear stress magnitude is computed as the time average over an entire cardiac cycle:

$$< |\mathbf{f}| >= \frac{1}{N} \sum_{i=1}^{N} |\mathbf{f}_i|, \tag{19}$$

where N is the number of time-steps per cardiac cycle, and the oscillatory shear index (OSI) is defined as:

$$\mathrm{OSI} = \frac{1}{2} \left(1 - \frac{| < \mathbf{f} > |}{< |\mathbf{f}| >} \right). \tag{20}$$

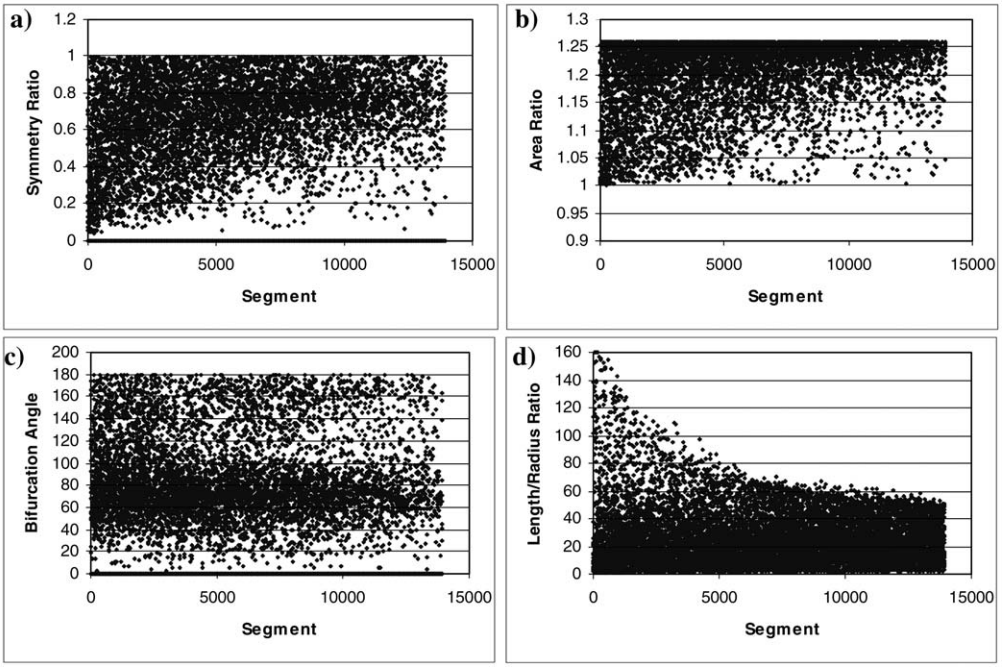

Figure 6. Statistics of geometrical properties of arterial trees generated using an image-based constrained constructive optimization method: a) symmetry ratio; b) area ratio; c) bifurcation angle; d) length-to-radius ratio.

Finally, another visualization technique that provides very intuitive information to the clinicians consists in simulating the passage of a contrast agent through the arterial model [41]. The time evolution of the concentration of a bolus of "virtual dye" is computed by solving the transport equation:

$$\frac{\partial C}{\partial t} + \mathbf{v} \cdot \nabla C = k \nabla^2 C, \tag{21}$$

where C is the concentration, $\mathbf{v}$ the velocity field and k the diffusivity constant. The solution is advanced in time for several cardiac cycles using the velocity field stored for one cardiac cycle. A time-dependent concentration is prescribed at a boundary simulating the injection of the contrast agent (Dirichlet conditions). On the remaining boundaries a zero normal derivative of the concentration is prescribed (Neumann conditions). Equation (21) is numerically solved using a stabilized finite-element formulation similar to the one used for the flow equations. The discretized finite-element equation can be written as:

$$\begin{aligned} \frac{1}{\delta t}\left[(C^{n+1,i}, q) - (C^n, q)_{\Omega^n}\right] + (\mathbf{v}^{n+1} \cdot \nabla C^{n+1,i}, q) + (k \nabla C^{n+1,i}, \nabla q) + \\ (\tau\, \mathbf{v}^{n+1} \cdot \nabla q, \mathbf{v}^{n+1} \cdot \nabla C^{n+1,i} - \xi^{n+1,i-1}) = (k \nabla C^{n+1,i}, q)_{\Gamma^{n+1}}, \end{aligned} \tag{22}$$

where q denotes the finite-element shape functions, $\tau = h^2/4k$ is the stabilization parameter, and the projection of the convective term ξ is obtained from:

$$(q, \xi^{n+1,i}) = (q, \mathbf{v}^{n+1} \cdot \nabla C^{n+1,i}). \tag{23}$$

In this way, "virtual angiograms" can be produced and presented to the physician using either surface plots of the concentration or volume rendering techniques. These visualizations

help one see regions of low flow (they are filled later and emptied later), regions of high flow (filled earlier, emptied quickly) and complex flow recirculations and secondary flow motions.

3. Results

A model of the circle of Willis of a normal volunteer was constructed from MRA image data. The images consisted in 98 slices of 256×256 pixels. Intensity levels were represented by 16 bits unsigned integers. Pixel size was 0·625 mm and the slice thickness was 1·6 mm. The anatomical model was constructed using the component-based approach described earlier. Each arterial branch was independently reconstructed using the tubular deformable model. Due to limited resolution, the anterior communicating artery (AcoA) was reconstructed in a slightly different manner. First, the image was cropped to reduce its size. Secondly, it was refined in all three dimensions so as to obtain a several pixels across the lumen. Then, the vessel axis was manually selected and the artery reconstructed using the deformable model. Once all branches were reconstructed, they were merged using four levels of background grid refinement (see Figure 2). A finite-element grid was then generated that contains approximately 1 million tetrahedral elements and 200,000 nodes (see Figure 3b).

Flow velocities were measured in the internal carotid arteries (ICA), the basilar artery (BA), the anterior cerebral arteries (ACA) and the middle cerebral arteries (MCA). The PC-MR images consisted in 32 phases (time frames) of 256×256 pixels. Pixel intensities were represented by 16 bits signed integers. The pixel size was 0·546875 mm and the slice thickness was 5mm. Each imaging plane was manually selected to be roughly perpendicular to the vessel axis. Flow rates were obtained using the cross-correlation method, and used to impose velocity boundary conditions in all these arterial branches. Traction-free boundary conditions were prescribed at the remaining outlets of the model, *i.e.*, the left and right posterior cerebral arteries (PCA). A CFD simulation was then performed using the non-Newtonian model of Casson. Periodicity in the pulsatile flow field was achieved in less than two cardiac cycles.

The computed flow field was then used to simulate the injection of a contrast agent into the right ICA. A bolus of dye of a Gaussian shape was prescribed at the inlet of the ICA. The time evolution of the dye concentration was calculated for several cardiac cycles assuming flow periodicity. Figure 7 shows snapshots of the dye concentration during the passage of the bolus. The top row shows dye concentration on the surface of the finite-element model. Volume renderings of the dye concentration, *i.e.*, intensity and transparency proportional to dye concentration, are presented in the bottom row. These "virtual angiograms" clearly show which feeding vessels are supplying blood to different regions of the brain. In particular, it can be seen that the right ICA supplies blood not only to the right MCA and right ACA but also to the left ACA through the ACoA. It can also be seen that during part of the cardiac cycle, blood is flowing through the right posterior communicating artery (PCoA) from the posterior to the anterior part of the circle of Willis, and then in the opposite direction.

The vascular bed model based on a series of resistors in parallel was then evaluated using the results of the CFD simulation. For each model outlet, a mean pressure was obtained during the CFD calculation. The flow resistance from the model outlet to the capillary bed was then obtained dividing this mean pressure by the mean flow through that arterial branch. These flow resistances were then compared to the resistances estimated using the series of resistors as explained by Cebral *et al.* [5]. The results are presented in Figure 8. It can be seen that this vascular bed model tends to underestimate the flow resistances in the MCAs and the PCAs

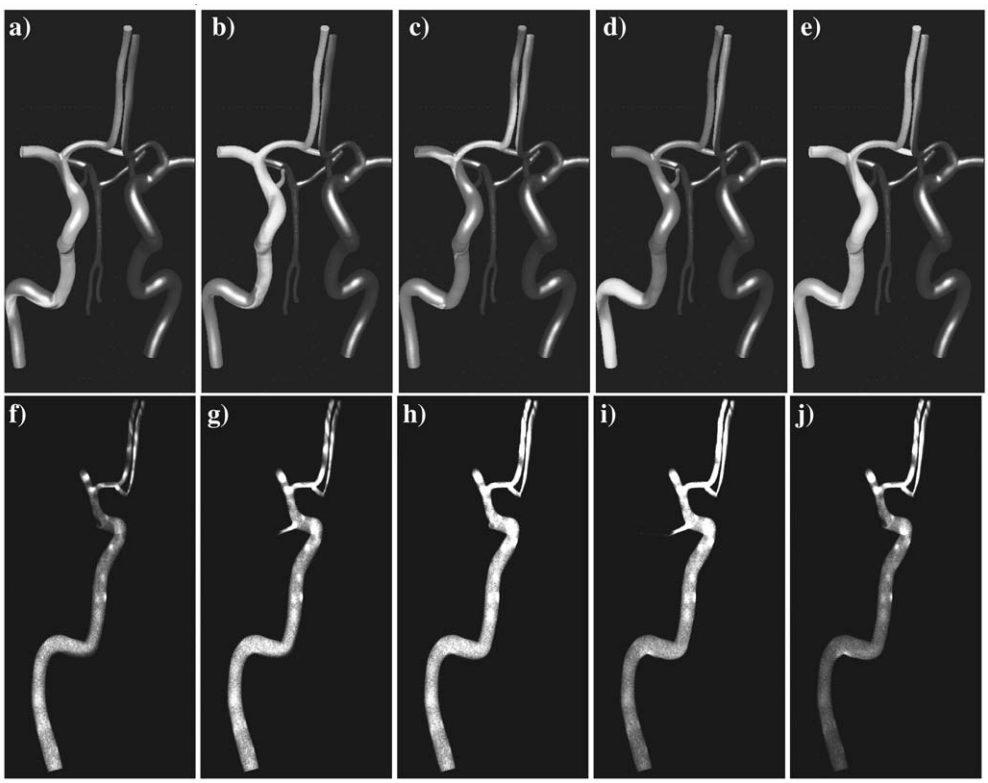

Figure 7. Flow visualization using "virtual angiograms". Top row: snapshots of dye concentration on the surface of the model. Bottom row: volume rendered concentrations during the simulation of the passage of the bolus of contrast agent.

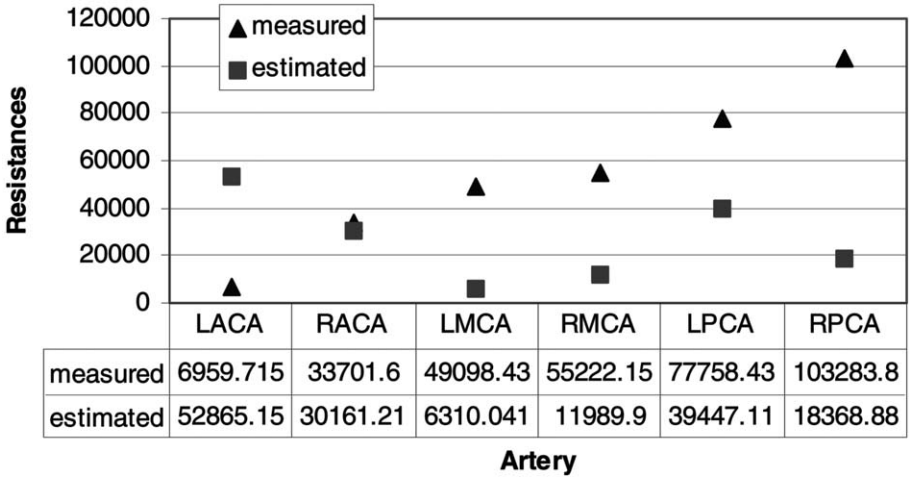

	LACA	RACA	LMCA	RMCA	LPCA	RPCA
measured	6959.715	33701.6	49098.43	55222.15	77758.43	103283.8
estimated	52865.15	30161.21	6310.041	11989.9	39447.11	18368.88

Figure 8. Comparison of flow resistances calculated from the CFD simulation (triangles) and computed using the vascular bed model based on parallel resistors (squares).

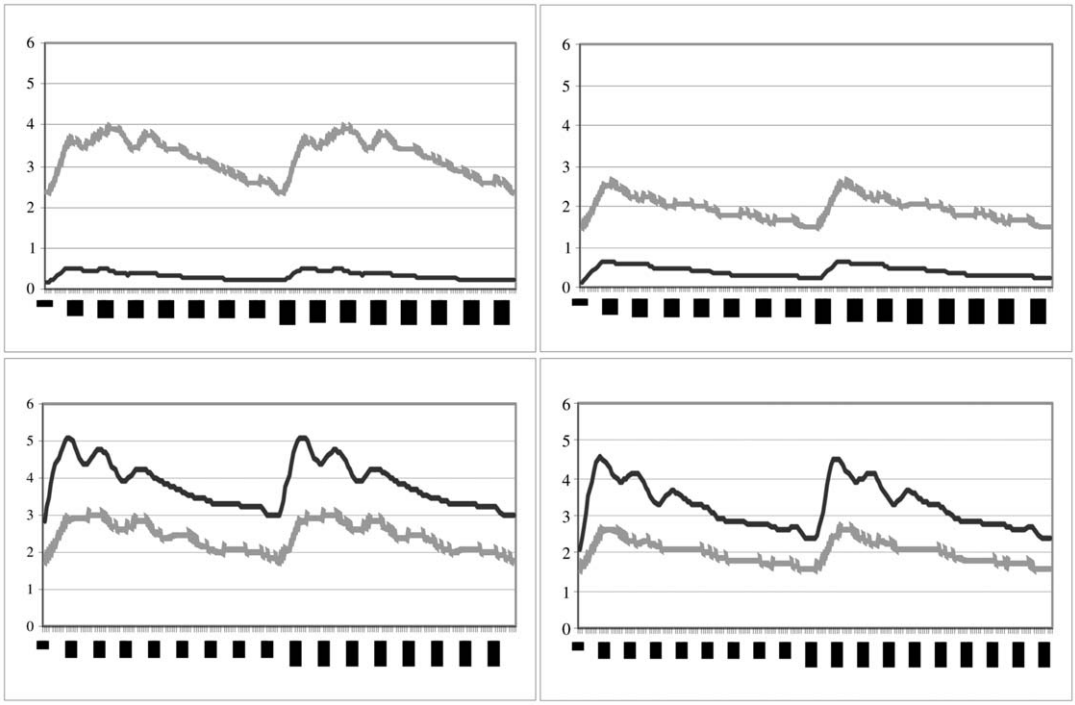

Figure 9. Comparison of flow rates (ml/s) obtained using boundary conditions derived from the vascular bed model (full red lines) against measured flow rates (dashed blue lines): a) left ACA; b) right ACA; c) left MCA; d) right MCA.

while it gives an overestimation of the resistance of the left ACA and a very good match to the right ACA. The goal of these vascular bed models is to prescribe pressure boundary conditions of the form $p = Q.R$ when flow measurements are not available. Therefore a new CFD simulation was conducted imposing these boundary conditions in all the outlets. Figure 9 presents a comparison of the computed (dashed lines) against the measured (full lines) flow rates through the ACAs and the MCAs. As expected, the calculated flow rates are higher in the ACAs and lower in the MCAs.

Finally, for comparison purposes a third CFD calculation was performed using a Newtonian fluid model and imposing the measured flow conditions. The results were post-processed and the mean WSS and OSI were computed. The regions of low mean WSS (less than 10 dyne/cm^2) are shown in Figures 10a, 10b and 10c for the Casson fluid, the Newtonian fluid with measured boundary conditions and the Newtonian fluid with boundary conditions from the vascular bed model, respectively. Similarly, Figures 11a, 11b and 11c show the corresponding distributions of OSI. Regions of vessel branching and high curvature exhibit high OSI and low mean WSS. These regions have been associated with localization atherosclerotic plaque and aneurysm development [42, Chapter 2]. The patterns of wall shear stress obtained with both the Newtonian and Casson models under measured flow conditions agree quite well. However, slightly higher OSI and lower WSS are obtained with the Newtonian model. Imposing boundary conditions from the vascular bed model causes differences in both the mean WSS and OSI distributions. The main discrepancies are observed in the ACoA and at the anastomoses of the PCoAs. This is a direct consequence of the change in the flow rates through each arterial branch.

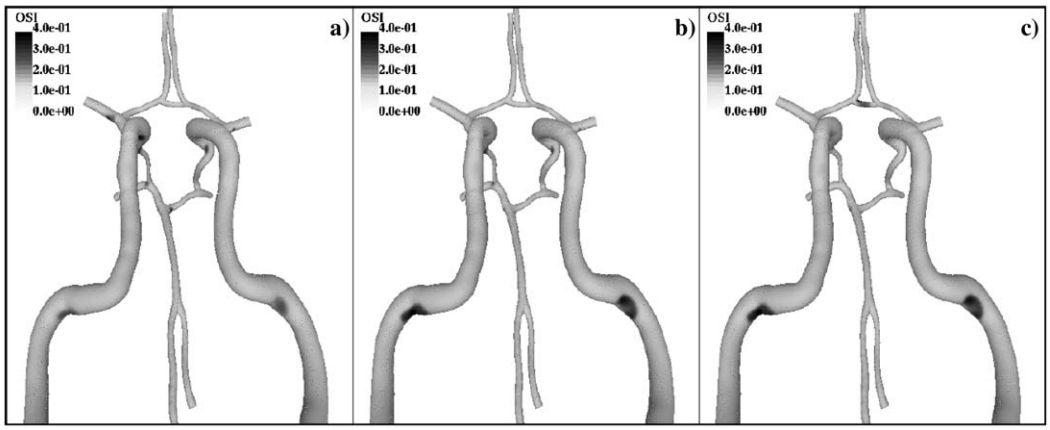

Figure 10. Comparison of regions of low mean wall shear stress magnitude ($<$10 dyne/cm^2): a) Casson fluid; b) Newtonian fluid; c) Newtonian fluid and vascular bed model.

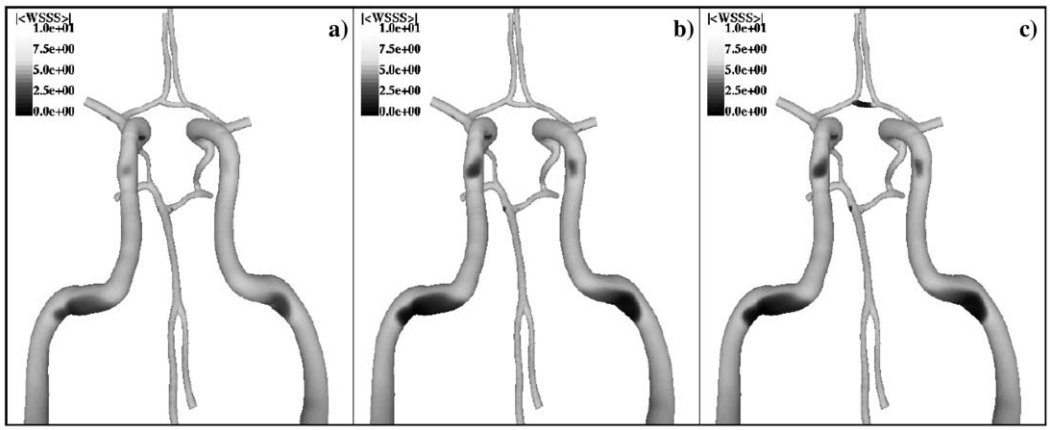

Figure 11. Comparison of oscillatory shear index: a) Casson fluid; b) Newtonian fluid; c) Newtonian fluid and vascular bed model.

4. Discussion

An image-based methodology for constructing patient-specific models of the cerebral circulation has been presented. This methodology combines anatomical and physiologic imaging techniques with computer simulation technology. The examples presented in this paper illustrate the methodology and represent a starting point in the development of more realistic models that can be applied to the study of cerebrovascular diseases and their treatment. Several challenging problems still remain to be solved. Anatomical modeling is a challenging problem, but several techniques are currently available to construct realistic models from medical images. Modeling arterial wall compliance is also a challenging problem. Fluid-solid coupling algorithms are available and have been used to simulate deforming vessels. However, the main difficulty lies in the specification of material properties of the arterial wall and the physiologic pressure waveforms that drive the wall motion. These quantities are difficult to measure non-invasively. The specification of physiologic flow conditions is another challenging problem, and perhaps the most complicated one. Flow waveforms can be

measured non-invasively using PC-MR or transcranial Doppler ultrasound (TCD) techniques. However, it is difficult to routinely obtain reliable flow measurements in all the afferent and efferent vessels of the circle of Willis. Therefore, the use of vascular bed or arterial tree models to prescribe outflow boundary conditions seems a promising approach. However, generating realistic patient-specific models of the microcirculation is a challenging problem, which is further complicated by autoregulation mechanisms. Perhaps the most challenging and important problem is that of *in vivo* validation. Measuring flow quantities that can be used to validate the computational models is difficult and usually requires complementary multi-modality imaging studies. Furthermore, several hemodynamics quantities such as wall shear stress cannot be reliably measured with current imaging technology. This is one of the reasons why computational models are being constructed in the first place. Another related question is that of how accurate do the computational models need to be. Some authors [43] have indicated that image-based CFD calculations do not need to be extremely accurate to provide useful clinical information. While this is an encouraging statement, one must be careful as to what effects are important and cannot be neglected in different applications. Finally, the development of computational tools that are fast enough and easy to use in routine clinical practice is a challenging problem. Automation and streamlining of the model construction process, scalable models, distributed computing and visualization systems, are among the key aspects that need to be addressed.

Our immediate work will focus in continuing refining the modeling methodology to incorporate arterial compliance, use 1D arterial tree models to specify outflow conditions, couple to autoregulation models, and develop tissue perfusion models. A substantial effort will be devoted to validation from multi-modality image data. We hope to apply these techniques to the study of cerebrovascular diseases and predicting the effects of endovascular procedures such as angioplasty and stenting, and local drug delivery.

Acknowledgements

Dr. Juan R. Cebral thanks the Whitaker Foundation for financial support.

References

1. G. W. Petty, R. D. Brown, J. P. Whisnant, J.D. Sicks, W. M. O'Fallon and D.O. Wiebers, Ischemic stroke subtypes; a population-based study of functional outcome, survival, and recurrence. *Stroke* 31 (2000) 1062–1068.
2. M. Kluytmans, J. van der Grond, K.J. van Everdingen, C. J. M. Klijn, L.J. Kappelle and M.A. Viergever, Cerebral Hemodynamics in Relation to Patterns of Collateral Flow. *Stroke* 30 (1999) 1432–1439.
3. R. M. K. W. Lee, Morphology of cerebral arteries. *Pharmac. Ther.* 66 (1995) 149–173.
4. R. H. Kufahl and M. E. Clark, A Circle of Willis Simulation Using Distensible Vessels and Pulsatile Flow. *J. Biomech. Engng*. 107 (1985) 112–22.
5. J. R. Cebral, R. Löhner and J. E. Burgess, Computer Simulation of Cerebral Artery Clipping: Relevance to Aneurysm Neuro-Surgery Planning. In: E. Oñate, G. Bugeda and B. Suarez (eds.), *Proc. ECCOMAS*, Barcelona, Spain, Sept. 11–14 (2000).
6. A. Fernandez, T. David and M. D. Brown, Numerical models of autoregulation and blood flow in the cerebral circulation. *Comp. Meth. Biomech. Engng.* 5 (2002) 7–20.
7. F. T. Charbel, K.H. Guppy, M. Zhao and M.E. Clark, Computerized hemodynamic evaluation of the cerebral circulation for bypass. *Neurosurg. Clin. N. Am.* 12 (2001) 499–508.
8. M. L. Barr and J. A. Kierman, *The Human Nervous System: an Anatomical Viewpoint*. Philadelphia: Lippincott Co. (1993), 451 pp.

9. J. A. Moore, D. A. Steinman, D. W Holdsworth and C. R. Ethier, Accuracy of computational hemodynamics in complex arterial geometries reconstructed from magnetic resonance imaging. *Ann. Biomed. Engng.* 27 (1999) 32–41.
10. C. A. Taylor, M. T. Draney, J. P. Ku, D. Parker, B. N. Steele, K. Wang and C.K. Zarins, Predictive medicine: vomputational techniques in therapeutic decision-making. *Comp. Assisted Surgery* 4 (1999) 231–247.
11. S. Z. Zhao, X. Y. Xu, A. D. Hughes, S. A. Thom, A. V. Stanton, B. Ariff and Q. Long, Blood flow and vessel mechanics in a physiologically realistic model of a human carotid arterial bifurcation. *J. Biomech.* 33 (2000) 975–984.
12. J. R. Cebral, P. J. Yim, R. Löhner, O. Soto and P. L. Choyke, Blood flow modeling in carotid arteries using computational fluid dynamics and magnetic resonance imaging. *Acad. Radiol.* 9 (2002) 1286–1299.
13. P. J. Yim, J. R. Cebral, R. Mullick and P. J. Choyke, Vessel surface reconstruction with a tubular deformable model. *IEEE Trans. Med. Imag.* 20 (2001) 1411–1421.
14. N. J. Pelc, Flow quantification and analysis methods. *MRI Clin. N. Am.* 3 (1995) 413–424.
15. C. J. G. Bakker, R. M. Hoogeveen and M. A. Viergever, Construction of a protocol for measuring blood flow by two-dimensional phase-contrast MRA. *J. Magn. Reson. Imaging* 9 (1999) 119–217.
16. B. R. Mustert, D. M. Williams and M. R. Prince, In vitro model of arterial stenosis: correlation of MR signal dephasing and trans-stenotic pressure gradients. *J. Magn. Reson. Imaging* 16 (1998) 301–310.
17. S. J. Owen, A survey of unstructured mesh generation technology. *Proc. 7th International Meshing Roundtable*, Sandia National Lab. (1998) 239–267 (www.imr.sandia.gov).
18. R. Löhner, Automatic unstructured grid generators. *Finite Elem. Anal. Design* 25 (1997) 111–134.
19. J. R. Cebral and R. Löhner, From medical images to anatomically accurate finite element grids. *Int. J. Num. Meth. Engng.* 51 (2001) 985–1008.
20. J. R. Cebral, Realistic modeling of arterial hemodynamics from anatomic and physiologic image data. In: R. C. Batra and E.G. Henneke (eds.), *Proc. 14th U.S. National Congress in Theoretical and Applied Mechanics*, Blacksburg, Virginia, June 23–28 (2002) p. 79.
21. J. R. Cebral, R. Löhner, P. L. Choyke and P. J. Yim, Merging of intersecting triangulations for finite element modeling. *J. Biomech.* 34 (2001) 815–819.
22. P. J. Yim, J. R. Cebral, R. Löhner, V. B. Ho and P. L. Choyke, Estimation of mechanical stress on the carotid artery. *Biomed. Engng Annual Conf.*, Durham (N.C.), Oct 4–7 (2001).
23. G. Taubin, A signal processing approach to fair surface design. *Comp. Graphics Proc.* (1995) 351–358.
24. R. Löhner, Regridding surface triangulations. *J. Comp. Phys.* 126 (1996) 1–10.
25. J. Mazumdar. *Biofluid Mechanics.* Singapore: World Scientific (1992) 191 pp.
26. F. G. Basombrio, E. A. Dari, G. C. Buscaglia and R. A. Feijoo, Numerical experiments in complex haemodynamics flows. Non-Newtonian effects. *Proc. XI Congress on Numerical Methods and Their Applications ENIEF*, San Carlos de Bariloche, Argentina, Nov. 24–29 (2000).
27. K. Perktold. and G. Rappitsch, Mathematical modeling of local arterial flow and vessel mechanics. In: J. Crolet and R. Ohayon (eds.), *Computational Methods for Fluid-Structure Interaction.* Pitman Research Notes in Mathematics 306 (1994) pp. 230–245.
28. P. Neofitou and D. Drikakis, Non-Newtonian modeling effects on stenotic channel flows. In: E. Oñate, G. Bugeda and B. Suarez (eds.), *Proc. ECCOMAS CFD*, Swansea, Wales, U.K., Sept. 4–7 (2001).
29. O. Soto, R. Löhner, J. R. Cebral and R. Codina, A time-accurate implicit monolithic finite element scheme for incompressible flow problems. In: E. Oñate, G. Bugeda and B. Suarez (eds.), *Proc. ECCOMAS CFD*, Swansea, UK, Sept. 4–7 (2001).
30. Y. Saad, *Iterative Methods for Sparse Linear Systems.* Boston: PWS Pub. Co. (1996) 447 pp.
31. J. R. Cebral, R. Löhner, O. Soto, P. L. Choyke and P. J. Yim, Image-based finite element modeling of hemodynamics in stenosed carotid artery. *Proc. SPIE Medical Imaging* 4683 (2002) 297–304.
32. J. R. Cebral, P. J. Yim, R. Löhner, O. Soto, H. Marcos and P. L. Choyke, New methods for computational fluid dynamics of carotid artery from magnetic resonance angiography. *Proc. SPIE Medical Imaging* 4321 (2001) 177–187.
33. J. S. Stroud, S. A. Berger and D. Saloner, Numerical analysis of flow through a severely stenotic artery bifurcation. *J. Biomech. Engng.* 124 (2002) 9–20.
34. N. Alperin, S. Lee, PUBS: Pulsatile-based segmentation of lumens conductiong non-steady flow. *Magn. Reson. Med.* 49 (2003) 934–944.
35. J. R. Womersley, Method for the calculation of velocity, rate of flow and viscous drag in arteries when the pressure gradient is known. *J. Physiol.* 127 (1955) 553–563.

36. C. A. Taylor, T. J. R. Hughes and C. K. Zarins, Finite element modeling of blood flow in arteries. *Comput. Methods Appl. Mech. Engng.* 158 (1998) 155–196.
37. M. S. Olufsen, C. S. Peskin, W. Y. Kim, E. M. Pedersen, A. Nadim and J. Larsen, Numerical simulation and experimental validation of blood flow in arteries with structured-tree outflow conditions. *Ann. Biomed. Engng.* 28 (2002) 1281–1299.
38. L. Formaggia, F. Nobile, A. Quarteroni and A. Veneziani, Multiscale modeling of the circulatory system: a preliminary analysis. *Visual. Sci.* 2 (1999) 75–83.
39. R. Karch, F. Neumann, M. Neumann and W. Schreiner, Staged growth of optimized arterial tree models. *Ann. Biomed. Engng.* 28 (2000) 495–511.
40. M. Zamir, On fractal properties of arterial trees. *J. Theor. Biol.* 197 (1999) 517–526.
41. F. Calamante, P. J. Yim and J. R. Cebral, Estimation of bolus dispersion effects in perfusion MRI using image-based computational fluid dynamics. *NeuroImage* 19 (2003) 342–353.
42. L. R. Caplan. *Stroke: a clinical approach.* Boston: Butterworths (1986) 343 pp..
43. J. S. Milner, J. A. Moore, B. K. Rutt and D. A. Steinman, Hemodynamics of human carotid artery bifurcations: computational studies in models reconstructed from magnetic resonance imaging of normal subjects. *J. Vasc. Surg.* 28 (1998) 143–156.